Earth and Space Science

Correspondence to:

M. Rincón,
marta.rincon@urjc.es

Monitoring Volcanic and Tectonic Sandbox Analogue Models Using the Kinect v2 Sensor

M. Rincón[1] , **A. Márquez[1,2]**, **R. Herrera[1]**, **O. Galland[3]** , **J. Sánchez-Oro[4]**, **D. Concha[4]**, and **A. S. Montemayor[4]**

[1]ESCET, Área de Geología, Tecvolrisk Research Group, Universidad Rey Juan Carlos, Móstoles, Spain, [2]Departamento de Mineralogía y Petrología, Universidad Complutense, Madrid, Spain, [3]The Njord Center, Physics of Geological Processes (PGP), Department of Geosciences, University of Oslo, Oslo, Norway, [4]CAPO Computer Science, ETSII, Universidad Rey Juan Carlos, Móstoles, Spain

Abstract The measurement of surface deformation in analogue models of volcanic and tectonic processes is an area in continuous development. Properly quantifying topography change in analogue models is key for a useful comparison between experiment results and nature. The aim of this work is to evaluate the capabilities of the simple and cheap Microsoft® Kinect v2 sensor for monitoring analogue models made of granular materials. Microsoft® Kinect v2 is a video-gaming RedGreenBlue-Depth device combining an optical camera and an infrared distance measurement sensor. The precision of the device for model topography measurements has been quantified using 64 experiments, with variable granular materials materials and distance to the model. Additionally, we tested the capabilities of averaging several distance images to increase the precision. We have developed a specific software to facilitate the acquisition and processing of the Kinect v2 data in experiment monitoring. Our results show that measurement precision is material dependent: with clear-colored and fine-grained materials, a precision ~1.0 mm for digital elevation models with a 1.6 mm pixel size can be obtained. We show that by averaging ≥5 consecutive images the distance precision can reach values as low as 0.5 mm. To show the Kinect v2 capabilities, we present monitoring results from case study experiments modeling tectonics and volcano deformation. The Kinect v2 achieves lower spatial resolutions and precision than more sophisticated techniques such as photogrammetry. However, Kinect v2 provides a cheap, straightforward and powerful tool for monitoring the topography changes in sandbox analogue models.

1. Introduction

Analogue modeling has been established as a powerful tool for the study of geological phenomena since Hall (1815), who reproduced for the first time the folding of sedimentary strata by horizontal compression, and Hubbert (1937), who developed the theory of scale models to study geological processes. Designing properly scaled laboratory experiments has little meaning, however, without a thorough quantification by using precise monitoring techniques. Thus, a four-dimensional (4D) monitoring of analogue experiments is key for understanding the processes modeled in the experiments, and subsequently to better understand geological processes.

Tectonics and volcanism are two of the geological processes more frequently addressed by analogue modeling, using a great variety of approaches and materials (see e.g., reviews by Graveleau et al., 2012; Kavanagh et al., 2018; Roche & Carazzo, 2019 and Schellart & Strak, 2016). One of the commonly used set-ups are the so-called "sandbox" models. Granular materials are used in sandbox experiments to simulate the brittle-plastic Earth's crust, as opposed to gelatine experiments that are used to simulate the brittle-elastic crust (e.g., Kavanagh et al., 2013; Reber et al., 2020). Granular materials replicate the Coulomb brittle properties of crustal rocks at experimental conditions, as they fail by shear and/or tensile fracturing, and are ideal to simulate faulting (e.g., Abdelmalak et al., 2016; Poppe et al., 2021; Ritter et al., 2016).

As faulting induces topography change, a proper monitoring of topography changes is essential in sandbox experiments intended to study volcanic and tectonic processes: for example, thrusting sequences or transpressive structures (e.g., Toeneboehn et al., 2018) or deformation of volcanic edifices (e.g., Cecchi et al., 2005). This monitoring is also key for the potential application of analogue modeling for a better interpretation of geodetic data monitored at active volcanoes (e.g., Bertelsen et al., 2021; Galland, 2012; Guldstrand et al., 2017, 2018). In sandbox experiments involving fluid flow, monitoring must be continuous due to the impossibility to stop and restart the experiment. In addition, scaling arguments imply that some volcano experiments are rather short, that

is, a duration of few seconds/minutes, with surface changes occurring in seconds (see e.g., Galland et al., 2018; Kavanagh et al., 2018).

Recent technical developments resulted the design of high-rate and precise quantitative monitoring systems (see Section 2). Most open-source methods require specific software and hardware and some expertise in device calibration and synchronization. To achieve this, the quantitative monitoring of analogue models can become a daunting task for some potential modellers who are not familiar with basic electronics and coding. Commercial packages can bypass such steep learning curve, but their elevated price makes them not affordable for the vast majority of academic laboratories.

In the last years, the release of RGB-D (RedGreenBlue-Depth) cameras has provided a simple and cheap option to produce high-rate, precise shape measurements. These cameras capture simultaneously optical images and distance-to-sensor images ("depth" or "distance" images) at high framing rates (e.g., Kadambi et al., 2014). Due to their primary use for video gaming, modern RGB-D devices exhibit high acquisition rate (several images per second), an easy use (plug-and-play devices) and do not require any previous calibration or subsequent image processing tasks. Probably the most popular RGB-D devices are the Microsoft® Kinect sensors, launched in 2010 for user interaction with the Xbox video-game console by gesturing detection. Thanks to their straightforward use and low cost, the applications of these sensors quickly extended to 3D scene reconstructions, robotics or medical applications (e.g., Dutta, 2012; Xia & Siochi, 2012).

Tortini et al. (2014) proposed the RGB-D Microsoft® Kinect v1 sensor as a novel technique for monitoring sandbox models. This low-cost device (100 US$ in 2013) captures simultaneously optical and distance images in near-real time (30 frames/sec) using a structured light pattern at a near-IR wavelength. Tortini et al. (2014) obtained successive digital elevation models (DEMs) of volcanic caldera collapse experiments with horizontal resolution and vertical precision of ∼1 mm, in agreement with other Kinect v1 applications (e.g., Wasenmüller & Stricker, 2016). These authors highlighted the easy use of both the device and the data it produces: distance-to-the-sensor images with millimeter-scale pixel size are obtained directly by an open-source software, so reducing data post-processing to a minimal.

In 2014 the Microsoft® launched the Kinect v2, with an improved distance sensor based on the Time-Of-Flight (TOF) technique using a laser and a near-IR camera, and a full-HD (High Definition) RGB camera (e.g., Gonzalez-Jorge et al., 2015; Sarbolandi et al., 2015). The Kinect v2 maintains the simplicity of use and the high rate data acquisition, and the low price (150 $US in 2014). Several tests of the Kinect v2 capacities show that distance images with a 1 mm resolution can be generated. However, the environmental conditions or the color and texture of the targeted materials influence the measurements (e.g., Ernst & Saß, 2015; Lachat et al., 2015).

The Kinect v2 device, with (a) its low price; (b) its easy use; (c) its high frame-rate (d) its full-HD RGB camera, and (e) its improved technology for acquiring distance data, has strong potential to successfully address the current challenges in monitoring volcanic and tectonic sandbox models and to overcome some of the problems of the existing methods (see Section 2). Its main unknown is the resolution/precision achievable by the device in sandbox models made of granular materials. Consequently, we designed a set of experiments to answer this question. Our aims are: (a) to evaluate the capabilities and potential advantages of the Microsoft® Kinect v2 device for monitoring topography changes in volcanic and tectonic analogue models made with granular material, (b) to provide a straightforward tool to optimize the monitoring of sandbox models with the Microsoft® Kinect v2, and (c) to design a simple but powerful processing method in order to improve the resolution of the measured topographic data.

2. Existing Methods for Topography Monitoring in Sandbox Models

Different methods are currently used for monitoring topography in volcanic and tectonic sandbox experiments with resolutions ≤1 mm. Laser scanners allow aquiring time series of DEMs with submillimeter resolution (e.g., Fittipaldi et al., 2019; Trippanera et al., 2015). However, the setup and acquisition time of laser scanners may take several minutes, during which the experiment must be stopped (e.g., Hatem et al., 2015; Pysklywec & Cruden, 2004). Laser scanners can therefore provide very good maps of the final topography change (e.g., Fittipaldi et al., 2019) or intermediate topography between experimental steps (e.g., Trippanera et al., 2015). However, laser scanners are not suitable dynamic topography recording at high rate (i.e., seconds).

Table 1
Characteristics of Kinect v2 Device

Technique	TOF
RGB sensor resolution	$1{,}920 \times 1{,}080$ px
Distance sensor resolution	512×424 px
Field of view RGB camera	$84.1° \times 53.8°$
Field of view distance camera	$70° \times 60°$
Maximum distance acquisition	4.5 m
Minimum distance acquisition	0.5 m
Frame per second (fps)	30 images/sec
USB	3.0
Supported OS	Windows 8

Note. TOF, Time-Of-Flight.

X-ray tomography scanners are also used for monitoring sandbox tectonic and volcanic models, allowing a 4D analysis of surface and subsurface deformation (e.g., Fedorik et al., 2019; Poppe et al., 2019; Rincón et al., 2018; Zwaan et al., 2020). However, the access to these scanners is not obvious, buying a scanner is very expensive, and the data volume and processing are challenging.

Modern optical methods for monitoring topography in sandbox models are mainly based on the semi-automated Structure-from-Motion (SfM) photogrammetric techniques (see e.g., Galland et al., 2016, and references therein). Time series of DEMs with a pixel size of ~0.1 mm, a vertical precision of ~0.05 mm and a high temporal resolution (up to 1 DEM per second) have been produced with this method, using 4–5 synchronized cameras (e.g., Galland et al., 2016; Grosse et al., 2020; Liu et al., 2019). However, the implementation of this methodology implies (a) an electronic knowledge to trigger several cameras synchronously, and/or (b) coding capacity for implementing non-user-friendly open-source software, or (c) a significant budget to buy costly commercial packages (in addition to the cameras/objectives).

Stereovision methodology, using only two cameras, can be used to compute sequential DEMs of model surfaces with an accuracy of ± 1 mm (Toeneboehn et al., 2018). However, a careful time-consuming calibration of the cameras and specific software for computing DEMs from the stereo-images are required. Similarly, using two cameras and a 3D Particle Imaging Velocimetry (PIV) system is possible to obtain 3D measurements of the model surfaces with a vertical accuracy of 0.1 mm (e.g., Schrank & Cruden, 2010). The required expertise and the price of the software needed for this method can be prohibitive for most modeling laboratories. Using one single camera and optical techniques based on structured light (also called moiré or fringe projection), Galland (2012) obtained DEMs with a good time resolution (1.5 s), a pixel size of <1 mm and a vertical accuracy of <0.2 mm. A complex implementation and processing are again required to obtain the DEMs from the raw images.

In summary, laser or X-ray scanners are not currently an easy and affordable option for monitoring fast topography measurements typical of some sandbox models. Optical photogrammetric methods can produce DEMs with horizontal and vertical resolutions ≤ 0.1 mm and time resolution up to 1 DEM/sec. However, these methods require the use of specific software and an implementation that can be challenging for geoscientists without electronic and/or coding training. This study provides an cheap and user-friendly alternative.

3. Experimental Method

Various parameters can affect the measurements with Kinect v2: (a) color and texture of the materials (e.g., Wasenmüller & Stricker, 2016), (b) the distance between the sensor and the experimental surface (e.g., Lachat et al., 2015), (c) potentially an existing topography as this could be a source of distortion of the results due to the used Time-of-Flight technology. In this study, we thus quantified the effects of the following parameters on the quality and robustness of topography measurements of the Kinect v2 in sandbox models: (a) influence of the material (texture and color); (b) distance from the sensor to the experiment; (c) effect of a topography. For the design of the experiments, let us consider the characteristics of the sensor and the data it produces.

3.1. The Kinect v2 Sensor Specifications

The Microsoft® Kinect v2 is a distance measurement sensor based on the TOF principle. It acquires simultaneously, by two different cameras, RGB and distance images of $1{,}920 \times 1{,}080$ pixels and 512×424 pixels of resolution, respectively, with a nominal frequency of 30 images per second in continuous mode (Table 1). The working distance of the Kinect v2 sensor is between 0.5 and 4.5 m, with a field of view of $70° \times 60°$ (Table 1). To calculate the distances, the Kinect v2 sensor measures distance via a laser that emits a burst of near infrared (IR) light ($\lambda = 830$ mm). The signal is refracted onto the surveyed surface, and the sensor measures the time delay between the emitted and received signal. Each pixel value of a measured distance image is the distance between the plane of the sensor and the observed object, in millimeters.
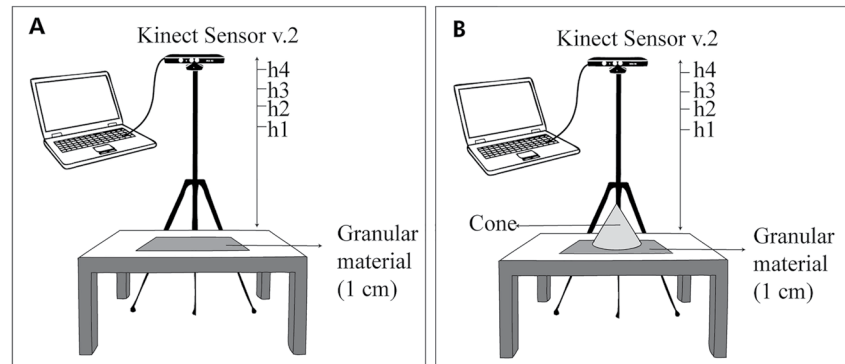
Figure 1. Experimental design used for (a) flat-surface experiments and (b) cone-topography experiments.

The distance images measured with the Kinect v2 distance camera exhibits a noisy aspect when analyzed in detail (see e.g., Jiao et al., 2017), which highlights accuracy limitations of the sensor. This results from unstable and oscillating two-way travel time measurements of the IR signal: even with a fixed distance between the sensor and the object, measured two-way travel time is exhibit small variations and swings with time (see e.g., Lachat et al., 2015). The time variations of the pixels of an image are similar but not synchronous, thereby pixels with the exact same distance can provide slightly different values, producing the noisy pattern observable in the distance images. Therefore, a fundamental task when analyzing the capabilities of the Kinect v2 sensor for providing reliable data for monitoring the small topographic changes produced at sandbox analogue models is the quantification of those oscillations of the values of the distance pixels.

Since the most important task in monitoring volcanic and tectonic sandbox analogue models is to measure time changes in the surface morphology, in this work we focus on evaluating the precision of the distance measurement, more than its accuracy. The International Metrology Vocabulary, in its third edition (2012), defines measurement accuracy as "the proximity between a measured value and a true value of a measured," that is, a measurement is more accurate when the measurement error is smaller. In the same text, precision is defined as "the proximity between the measured values obtained in repeated measurements of the same object, or of similar objects, under specific conditions." The precision of a measurement depends only on the distribution of random errors during acquisition and has no relationship to the actual value. The concept of precision always denotes repeatability and it is usually expressed numerically by dispersion measurements, such as standard deviation, variance or coefficient of variation.

In this work, to evaluate the precision of the distance measurements acquired by the Kinect v2 sensor, we used 40 consecutive distance images of a fixed object, and we calculated an average image. We then calculated residual images by substracting each of the 40 images with the average image, and computed the standard deviation of all the pixels of the 40 residual images as a proxy of the measurement precision. Thus, the lower the standard deviation, the higher the precision reached by the Kinect v2 distance data. That value of the standard deviation provides an estimate of the topography change detectable by the device with the tested parameters.

3.2. Experimental Design

We ran a set of 64 experiments with the following variables: 8 materials at 4 distances with 2 topographic settings (Figure 1). In each experiment, we compute the measurement precision as described in the previous section.

We used a graduated tripod to hold the Kinect v2 sensor, which pointed sownward, at controlled distances above a horizontal table, where the tested materials were placed (Figure 1). The Kinect sensor was connected to a USB-3 capable to a computer, which controlled data acquisition, and where the RGB and distance images were downloaded (see Section 3.4). In each of the tests, distance images were acquired at a frequency of one image per second during 200 s.

The distance of the Kinect sensor to the measured surface controls: (a) the pixel size (i.e., the spatial resolution) in both distance and RGB images, and (b) the size of the experiment. The shorter the distance between the sensor and the experiment, the higher the pixel resolution, but the smaller the maximum experiment size. In this work, the Kinect

Table 2
Distances Kinect-Experiments Used, and Experiment Size and Images Characteristics for Each Distance

Name	Height (mm)	Maximum size of the experiment (m)	Pixel size of distance image (mm)	Pixel size of RGB image (mm)
h1	600	0.84 × 0.69	1.64 × 1.63	0.44 × 0.64
h2	750	1.05 × 0.87	2.05 × 2.04	0.55 × 0.80
h3	900	1.26 × 1.04	2.46 × 2,45	0.66 × 0.96
h4	1,005	1.47 × 1.21	2.75 × 2.74	0.73 × 1.07

v2 data were acquired at 4 different heights, between 0.6 and 1 m (Table 2; Figure 1). The pixel and experiment sizes for the 4 different sensor heights used in this work, are calculated from the resolution and field-of-view values of the Kinect v2 camera and shown in Table 2. The theoretical minimum acquisition distance of the Kinect v2 sensor is 0.5 m, however at that distance our measurements provided numerous invalid pixels (with value NaN), showing that the sensor was not able to record meaningful measurements with such distance. Thus, we chose the minimum height of the device at 0.6 m. Conversely, although the Kinect sensor has the ability to acquire data up to a distance of 4.5 m, and therefore monitor experiments up to a size of 6.30 × 5.20 m, the maximum acquisition distance in this work was 1.05 m since we did not find examples of sandbox experiments larger than 1.2 m in the literature.

Using this experimental design (Figure 1), we monitored the surface of eight different granular materials (see Section 3.3) at each of the four different heights selected. Finally, we tested the effect of topographic distortion on the measurements by comparing flat models with a 1 cm-thick layer of granular material (type A) to models with a cone (5 cm high, 23 cm diameter) resting on a basal layer of the same granular material (type B) (Figure 1).

3.3. Materials

We evaluate the influence of the grain size, texture and color of the granular material used in sandbox experiments on the precision of the Kinect v2 device for monitoring sandbox models. We expect to determine how the reflectivity of each material can affect the precision of the distance images and if they are suitable to be monitored with the Kinect sensor. The materials tested (Table 3) are similar to those used previously in experiments for volcano-tectonic analogue modeling, such as plaster (e.g., Von Hagke et al., 2019), diatomite (e.g., Gressier et al., 2010), feldspar sand (e.g., Agostini et al., 2009), silica sand (e.g., Abdelmalak et al., 2016; Schellart, 2000) or sand-plaster mixture (e.g., Poppe et al., 2021; Roche et al., 2001).

We used six granular materials (Table 3) with variable composition, color and grain size and distribution: two fine-grained powders (Plaster and Diatoms), one fine-grained sand (Feldspar sand, with two different colors), one intermediate-grain size sand (Sand "Ebro"), one medium-grain size sand (Quartz sand "(SIL)" with two different colors) and a quartz sand - plaster mixture with 80/20 mixing proportion. All of them are commercial materials, except the natural sand collected from the Ebro Delta (Spain). The two materials with the smallest grain size are the diatomite and plaster powders, both white in color, with a similar mean value of around 2 μm, but with different compositions (siliceous diatoms and calcium sulphate hemihydrate, respectively). The finest sand is the feldspar sand (grain size 1–300 μm). Its natural color is white, but we have also dyed it in blue in order to test the color effect (Table 3). The Ebro Delta sand is an intermediate grain-size sand (63–250 μm), with a better sorting than the feldspar sand, and a speckled color pattern due to lithological variety. The quartz sand is our coarsest grain-size sand (125–425 μm), and we colored it green and black (again to test the possible effect of the material

Table 3
Characteristics of the Different Materials Tested

Name	Material type	Grain size (μm)	Grain size (μm) D50	Cu	Heterometry	Roundness	Color
PLASTER	Plaster powder	≤2		-	Low	-	White
DIAT	Diatoms	≤2		-	Low	-	White
FEL_WHITE	Feldspar sand	1–300	45	9	Intermediate	Low	White
FEL_BLUE	Feldspar sand	1–300	45	9	Intermediate	Low	Blue
SIL_GREEN	Silica sand	125–400	313	0,8	Low	High	Green
SIL_BLACK	Silica sand	125–400	313	0,8	Low	High	Black
EBRO	Ebro Delta sand	63–250	190	0,6	Low	Variety	Speckled
SIL + PLASTER	Silica sand + Plaster volume ratio 4:1	63–250	170	0,5	Bimodal	Low	White

Note. FEL, fine-grained sands; SIL, Quartz sand.

color). Finally, the white plaster-silica sand mixture has a grain-size that is intermediate between those of the feldspar sand and the Delta Ebro sand, but with lower sorting (Table 3).

3.4. Data Acquisition: KAM Software

The Kinect v2 for Windows is a Microsoft plug-and-play device which can be easily driven by using a free set of tools downloadable from the Microsoft web site, as well as several other free tools such as for example, RGB-D (see Tortini et al., 2014) or Kin2 for Matlab (Terven & Córdova-Esparza, 2016). A simple but useful software designed specifically to record the Kinect v2 data from sandbox analogue models has been developed by the CAPO research group from Rey Juan Carlos University in the framework of this work: the Kinect Acquisition for Analogue Models (KAM) software. The aim for developing KAM software is to help modellers to use the Kinect v2 device for monitoring topography change in analogue models. KAM is a free and stand-alone software, and is publicly available at https://github.com/capo-urjc/KAM (https://doi.org/10.5281/zenodo.3956392).

The software runs on Windows 7/10 using the Microsoft Kinect For Windows SDK 1.8. The package contains several tools to facilitate the acquisition and processing of the data obtained with the Kinect v2 sensor. One of the improvements of our software is the possibility to replace the RGB camera of the Kinect v2 device by any other digital camera connected to the computer. In this way, the pixel resolution of the RGB images of the experiment surface can be enhanced. We tested the software using a Logitech c920 webcam (1,920 × 1,080 pixels images and optical zoom), obtaining RGB images with a pixel resolution of up to ≈0.2 mm, synchronized with the distance images. Another useful tool is the possibility to control the frame-rate at which both the RGB and distance images are acquired. The RGB images and the distance images are recorded in distinct folders.

KAM records the distance data on the hard drive of the computer as images with a raw binary format (files without extension). This facilitates the later working with the most commonly used programmes in the study of natural processes in analogue models (e.g., Matlab, Arcgis, Image-J, Python). In this way, the post-processing required to use distance images to build DEMs and deformation maps is minimal: simple import of the files as 512×424, 16-bit unsigned files, is enough to get distance images with the pixel value in millimeters (an example using Image-J is included in the KAM software manual).

In analogue modeling of geological processes, time is an important parameter; therefore, KAM controls the exact time of acquisition of each image and saves it in two .txt files (one for RGB images and another for distance images) stored in the corresponding image folders. Since the characteristics of the computer will determine the rate of acquisition, we observed that, in some cases, the nominal maximum number of images per second as listed in the specifications of the Kinect v2 sensor (30 images/second), cannot be reached. This is due to bandwidth limitations in the storing process, especially if a mechanical disk is used. Note that the RGB image in Full-HD resolution ($1,980 \times 1,080 \times 3$ bytes/pixel, ×30 fps) results in a necessary data transfer rate of 178 MB/s, and the depth image ($512 \times 424 \times 2$ bytes/pixel, ×30 fps) results in another transfer rate of 12 MB/s, so a total of 190 MB/s. Although this is far below the theoretical 640 MB/s of a USB-3 bandwidth, a typical Hard Disk Drive (HDD) drive gives a maximum of 120 MB/s, which is below the needed frame-rate and, therefore, the bottleneck in our experiments. Cropping the captured image using KAM before storing could be interesting in some scenarios. Another strategy is to change the HDD to a faster Solid Estate Drive (SSD) drive or just reducing the acquisition frame-rate. For instance, by using a Dell Optiplex 9,200 computer (Intel Core i7-4,790 3.6 GHz, 8 GB RAM, SSD hard disk) we observed that a maximum frame-rate of only 10 images per second can be recorded on the computer disk.

3.5. Data Processing

In our experiments, we observed (Figure 2) the temporal swinging nature of the pixel values typical of the Kinect v2 distance images (see Section 3.1). In order to reduce the resulting noise in the distance images, we used a time filtering method, by averaging several successive images. This method reduces the measurement noise (e.g., Lachat et al., 2015), avoiding the smoothing effect inherent to spatial filters, which could potentially reduce the actual deformation values, especially around sharp topographic features such as fault scarps.

To apply and optimize this time filtering, we proceeded as following:

1. Starting from an total number of *n* DEMs, we first calculated the standard deviation of the n data values for each pixel of the DEMs, and calculated their average standard deviation;
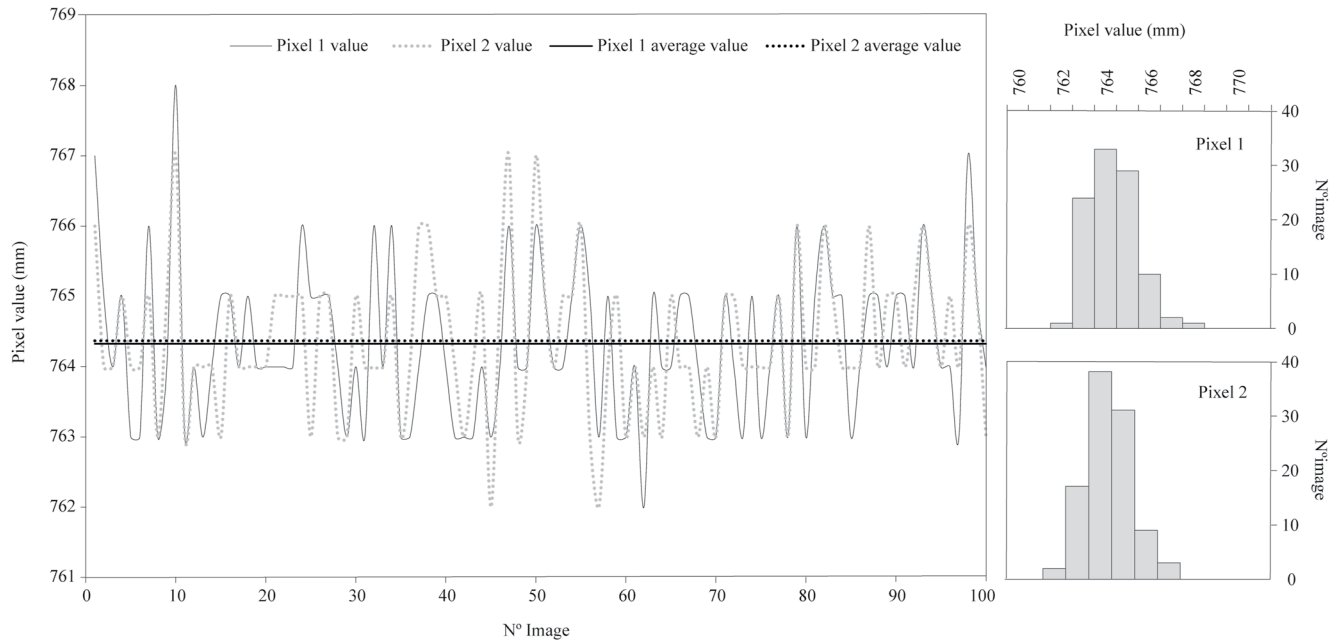
Figure 2. Temporal variation of distance values for two close pixels for 100 consecutive Kinect v2 distance images taken in a static experiment of granular material. Although the value of each pixel value swing over time up to 5 mm the average value of the two pixel are identical, as well as the value distribution show at the histograms.

2. Second, we grouped the n DEMs in groups of two, and calculated the averages of the DEM pairs. We then calculated the standard deviation of the values for each pixel of the averaged DEMs, and calculated their average standard deviation;

3. Third, we grouped the n DEMs in groups of three, and calculated the averages of the DEM triplets. We then calculated the standard deviation of the values for each pixel of the averaged DEMs, and calculated their average standard deviation;

4. We went on like this until grouping the n DEMs in groups of 10, calculating the averages of the DEM groups, and then calculating the standard deviation of the averaged DEMs.

In each step, we produced a total of $na =$ Total number of images/Number of averaged images. This data processing tool is implemented in our KAM software. This procedure will allow quantify how the precision of the pixel values of the images evolves when averaging several images.

4. Results

4.1. Influence of the Parameters

Fine-grained powder materials (PLASTER and DIAT) show the best precision (lower standard deviation values) for the distance images obtained with the Kinect 2 sensor, with values between 1.0 and 1.3 mm (Figure 3). As the acquisition distance increases, the standard deviation also increases (i.e., the precision is lower; Table 4; Figure 3). The fine-grained sands, as well as the sand-plaster mixture (SIL + PLASTER), show quite similar values and distance-precision trends than those of the powders (Table 4; Figure 3).

However, the intermediate grain-size sand EBRO, with a speckled colored pattern, shows an opposite trend for the distance-precision relationship: the standard deviation value for the lowest monitoring distance (600 mm) is 1.4 mm whereas for the highest distance (1,005 mm) is 1.2 mm (Figure 3), that is, the precision increases with increasing distance of the sensor.

The medium grain-size quartz sand colored in green (SIL_GREEN) shows values (and trend) quite similar to the white sand-plaster mixture, whereas the same material colored in black (SIL_BLACK) shows higher values:
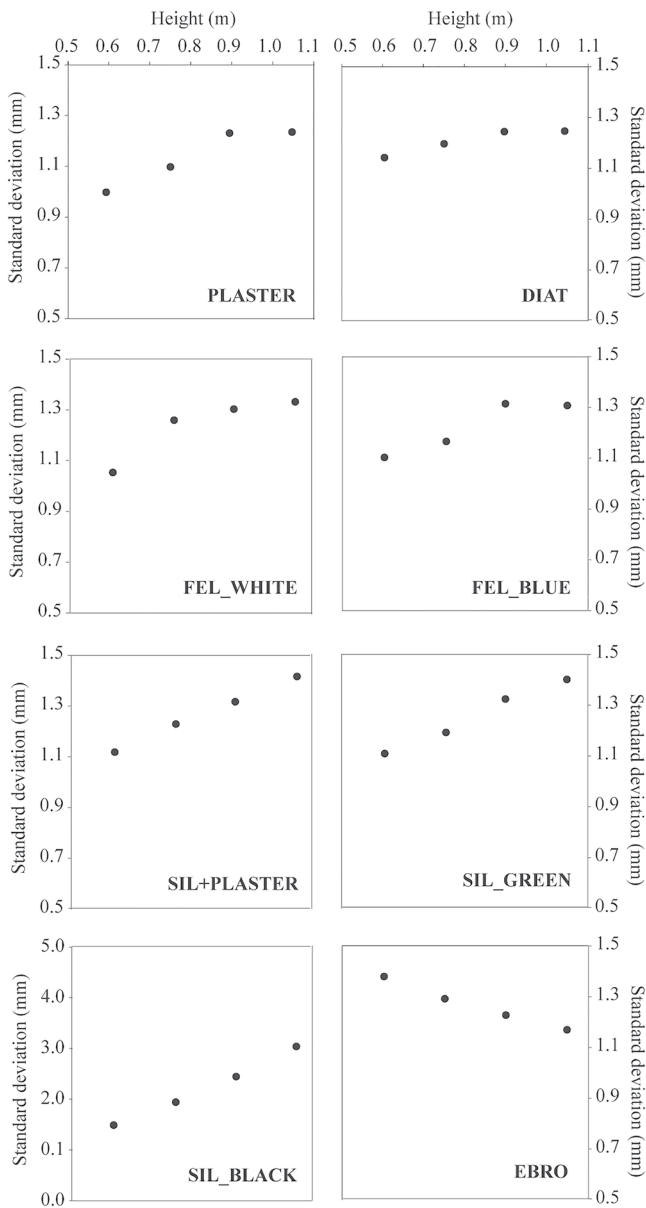
Figure 3. Standard deviation value of the distance for the different granular materials tested for each of the four distances used. Note that all the vertical scales are identical except that of Quartz sand (SIL)_BLACK material, which shows values much higher.

1.5 mm for a 600 mm monitoring distance but strongly increasing up to 3 mm at a distance of 1,005 mm (vs. 1.4 mm for SIL_GREEN) (Figure 3).

Finally, for all materials, both data acquired in experiments with a flat surface (type A) and with topography (type B) show very similar standard deviation values, with differences smaller than 0.1 mm for any working distance (Figure 4).

4.2. Processing Results

Figure 5 displays how the standard deviation evolves with increasing number of averaged images for the SIL_PLASTER and PLASTER granular materials. Our results confirm that the averaging of successive distance images measured by the Kinect v2 reduces the values of the standard deviation, and so increased the measurement resolution. Figure 5 also shows that the trend is not linear, with the fastest decrease occurring for the averaging involving up to five images (n5) (Figure 5). For example, for the plaster material the averaging of 2 consecutive images (n2) reduces the standard deviation by ~30% (from 1 to 0.7 mm) but the averaging of 5 images (n5) reduces it only 50% (Figure 5). This processing leads to precisions ≤0.5 mm for distance images obtained for powder and fine-grained sands (down to 0.3 mm for plaster). Our results also show that the averaging of more than 10 images does not further reduce the standard deviation values, since from 8 averages those values show only small variations (Figure 5).

4.3. Integration of Results: The Precision of the Kinect v2 Distance Images

We applied this averaging procedure to improve measurement precision to all materials tested in this study, and the results are displayed in Figure 6. A remarkable feature is that at the studied distances (between 0.6 and 1.05 m) for most of the materials, the precision of the distance images from the Kinect v2 device is lower than 1.5 mm and can be as low as <0.5 mm when image averaging is applied (Figure 6). We notice that two of the analyzed materials show distinct behaviors. First, while most trends exhibit lower precision for increasing distance, the EBRO sand shows the counterintuitive opposite result, that is, increasing precision with increasing distance (Figure 6). While we found no previous work showing this, we propose that it can be related to the diversity of size, angularity and color of the grains of EBRO sand, which likely influence the reflection of the IR light back to the Kinect v2 device. Second, the standard deviation values obtained in the different materials are very similar except for those obtained for the material SIL_BLACK, which are much higher. This confirms that the color of the granular material must be taken into account for monitoring sandbox experiments with the Kinect v2,

and that dark colors produce a much lower precision. However, this should not be a common problem since the most used granular materials in sandbox analogue models are usually white or light-colored (plaster, silica sand). In addition, the time-averaging filtering is very efficient to increase precision with this material, such that we can reach standard deviation value down to ≈0.5 mm by averaging 10 consecutive images (Figure 6).

Our analysis shows that DEMs of sandbox model surfaces with a pixel size of ~1.6 mm and a vertical precision ≤0.5 mm can be obtained very easily using the Kinect v2 with KAM. This vertical precision is close, but still lower, than precisions obtained by previous authors in similar experiments using more complex optical methods such as moiré projection (~0.2 mm; Galland, 2012) or photogrammetry (~0.05 mm; Galland et al., 2016). Note that time averaging is the resulting in time resolution decrease. Since only 10 distance images per second can be

Table 4
Standard Deviation Values (Sd) for All the Materials Tested at the Lowest and Highest Distances

Material	Height	Sd (mm)	ΔSd (mm)
PLASTER	h1	1.0	0.2
	h4	1.2	
DIAT	h1	1.1	0.2
	h4	1.3	
FEL_WHITE	h1	1.1	0.2
	h4	1.3	
FEL_BLUE	h1	1.1	0.2
	h4	1.3	
SIL + PLASTER	h1	1.1	0.3
	h4	1.4	
SIL_GREEN	h1	1.1	0.3
	h4	1.4	
SIL_BLACK	h1	1.5	1.5
	h4	3.0	
EBRO	h1	1.4	0.2
	h4	1.2	

Note. FEL, fine-grained sands; SIL, Quartz sand.

acquired with Kinect from a simple computer (see Section 3.4), a time-averaging filtering with 5 consecutive images (to reach ≤0.5 mm Z-precision DEMs) would lead to a time resolution of 2 DEMs per second. However, this time resolution is still better than those from optical methods (1 DEM per second).

5. Case Studies: Monitoring Tectonic and Volcanic Deformation Models With Kinect v2

Two case studies are presented here to show the capacity of the Kinect v2 device for monitoring topography changes in sandbox volcano-tectonic analogue models. In the Analog Modeling Laboratory of the Rey Juan Carlos University (LABMOA), we performed two different experiments: (a) a tectonic model reproducing a simple compressive shortening (Figure 7), and (b) a volcano-tectonic model where a viscous analog magma is injected in a stratovolcano (Figure 9). In both cases, we captured RGB and distance images using the Kinect v2 device located at 80 cm above the experiment using our KAM v2 software. We also implemented time-averaging filtering with the KAM v2 software to improve the precision of the model topography (see Section 4.2). We used Image-J load and display the measured DEMs (pixel ~ 2 mm), and to apply further analysis (i.e., differences between initial and final topography, spatial and temporal topographic profiles). The granulat material used in these two experiments was SIL + PLASTER (Table 3), because its mechanical propreties are suitable to produce both tensile and shear fractures (Poppe et al., 2021).

5.1. Tectonic Experiment

We reproduced one of the benchmark models of brittle thrust wedges by Schreurs et al. (2016), to compare our results with those from other 14 laboratories listed in this work. The experiment reproduces a simple shortening process due to compression (Figure 7a). The model width and length were 30 and 35 cm, respectively, and an initial thickness of 3 cm of SIL + PLASTER material was poured and flattened directly over the basal plate. Total shortening of the model by inward displacement of a mobile wall was 10 cm, at a constant velocity of 3 cm/hr. Using the Kinect v2 device, RGB and distance images at 10 s intervals were acquired during the entire experiment.

The Kinect RGB images of the experiment surface show the successive development of curved asymmetric positive reliefs, which are likely the surface expression of a sequence of thrust faults (Figure 7b). The final geometry of the model was similar to those performed at other laboratories (Figure 18 of Schreurs et al., 2016). The final DEM obtained from the Kinect v2 distance images shows an accumulated maximum uplift of ≈30 mm (Figure 7c). The standard deviation of the Kinect-derived DEM (obtained from the difference between the final distance image to the immediately previous one) is ≈1.5 mm, making the results noisy and speckled. We improved the DEM quality by applying time-avereging filtering of the 6 final consecutive distance images: the speckled pattern is reduced (Figure 7d) and the standard deviation decreases to ≈1.0 mm.

Monitoring during the experiment allows quantifying time evolution of the model topography. Figure 8a displays a profile across the center of the model of the topography difference between the final and initial times. It is also possible to quantify the time evolution of the elevation at one specific point throughout the entire experiment (Figure 8b).

5.2. Volcanotectonic Experiment

In this experiment, we built a cone of sand, in which we injected a viscous magma analog that well-characterized and commonly used in analogue models: Tate & Lyell Golden Syrup (e.g., Beckett et al., 2011). The base diameter of the cone was 30 cm, and its height was 11 cm to simulate a 1,100 m high volcanic edifice. The syrup
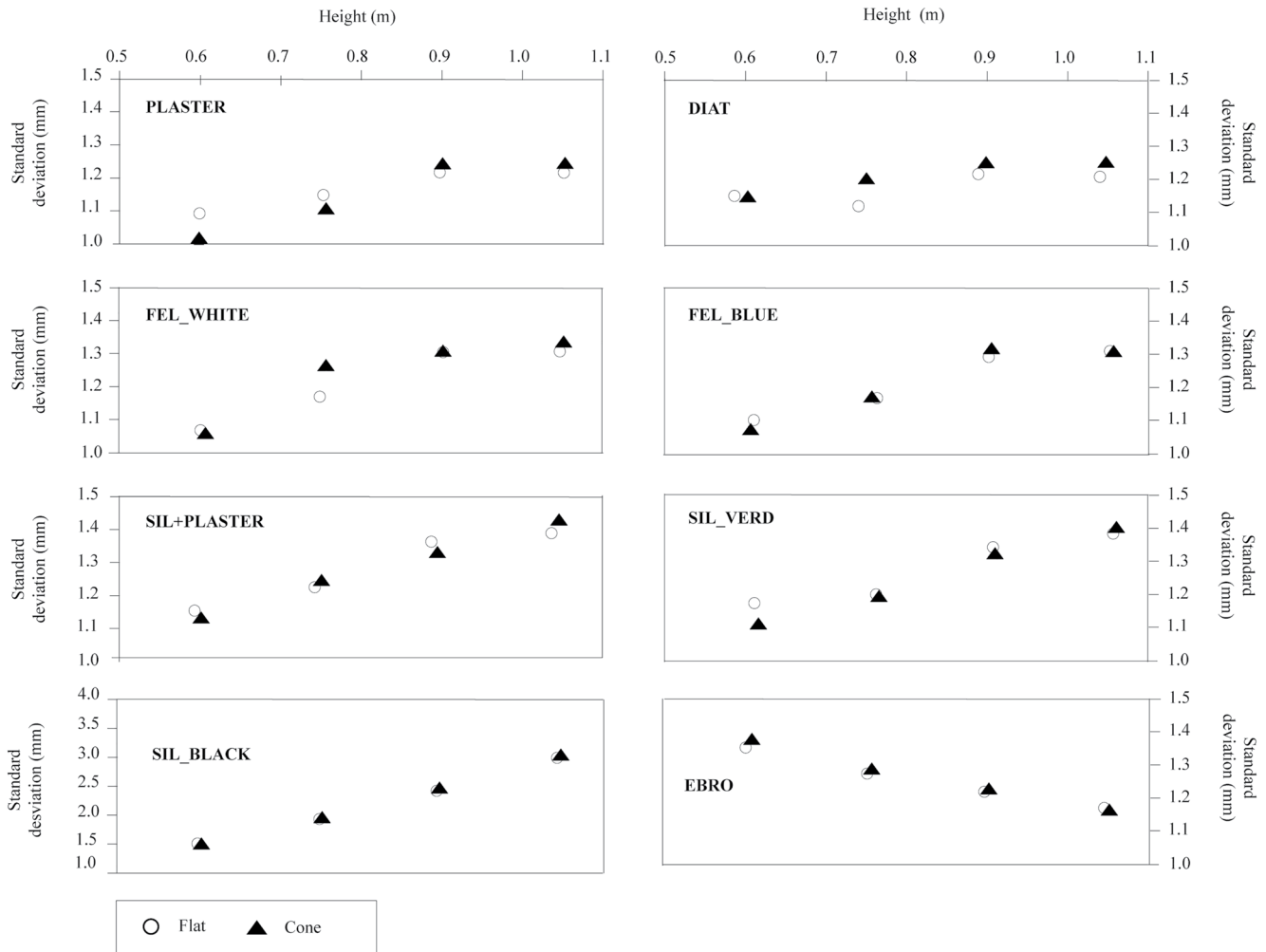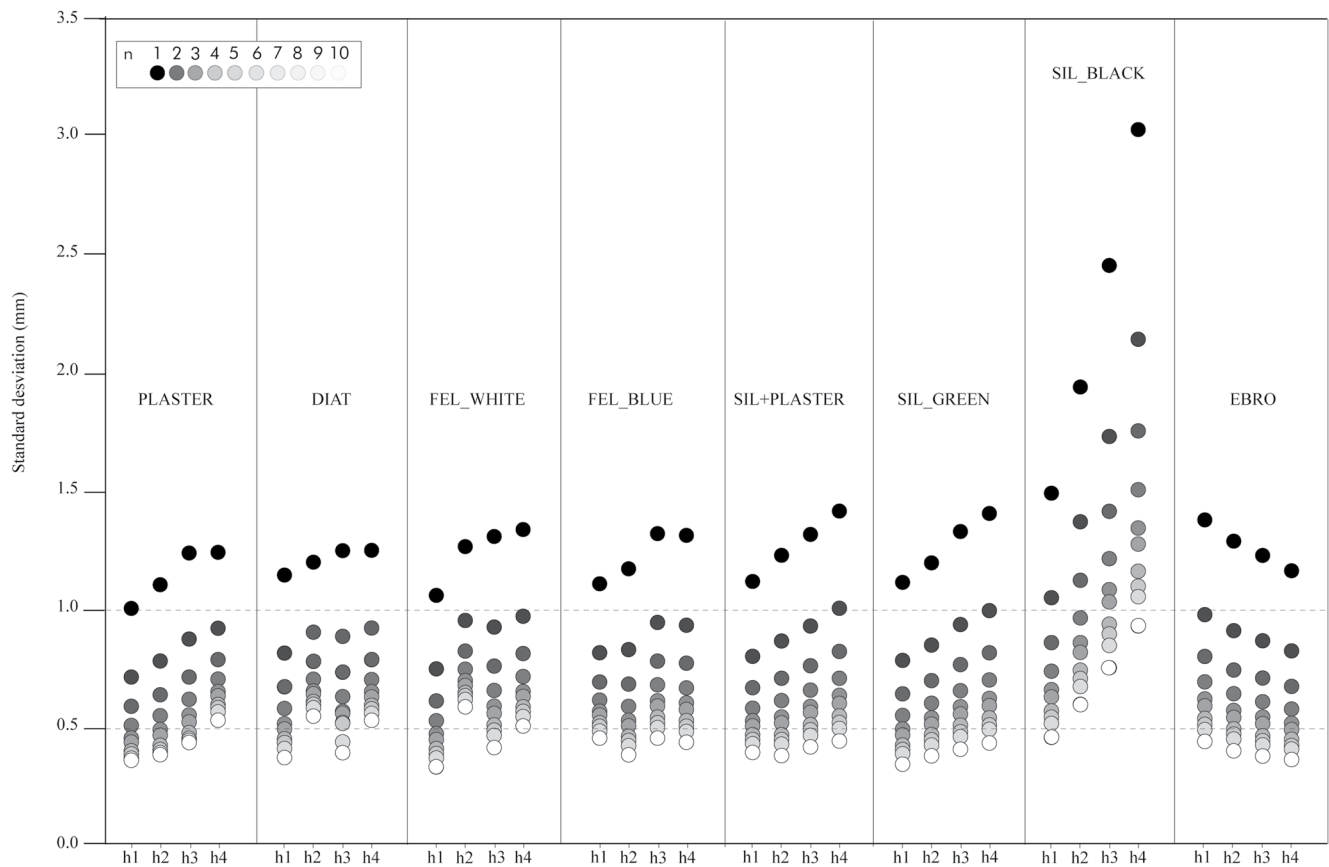
Figure 4. Comparison of the standard deviation values of the distance for each material and distance between the experiments with a flat surface and those with a cone. All the values are almost identical. Note again that the Quartz sand (SIL)_BLACK material has a different scale.

(viscosity 23–37 Pa·s) was intruded at the base of the stratovolcano by applying an overpressure induced by a syrup reservoir located 136 cm above the model base (Figure 9a). The model geometric ratio was 1:10,000 (i.e., 1 cm represents 1,000 m in nature) and 1 min of the experiment represents approximately 30 hr in nature (see Rincón et al., 2018 for materials and scaling details). The Kinect v2 device acquired one RGB and one distance images per second. The experiment duration was 70 min (i.e., simulating an 87 days-long intrusion), so that 4,200 distance images were recorded. The resolution of the obtained DEMs was 2 mm, corresponding to ∼20 m in nature.
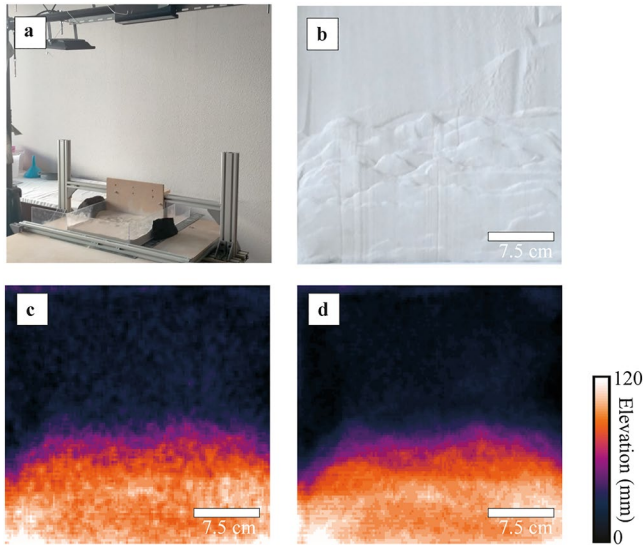
At the end of the experiment, the RGB image of the model allows mapping the volcanotectonic structures that deformed the volcano (Figure 9b): a curved fault-related scarp at one side marked an inward-dipping fault, plus a strongly fractured zone at the opposite upper flank of the volcano, which together seem to delineate an asymmetric half-graben affecting the volcano summit zone. Those features can also be observed in the DEM, especially the summit scarp (Figure 9c), even with the speckled pattern of that DEM. The standard deviation of the Kinect-derived DEM, calculated from the subtraction of the simple final distance image to the immediately previous one (just one second delay), is ≈1.5 mm that is, similar to that calculated in the tectonic experiment. We applied time-averaging filter on the 7 final consecutive images: the speckled pattern in the DEM is strongly reduced (Figure 9d) and the standard deviation decreases to ≈1.0 mm. The sharp topographic scarp produced by summit faulting is clearly visible in this DEM since the time-averaging filtering method does not smooth spatially the image.
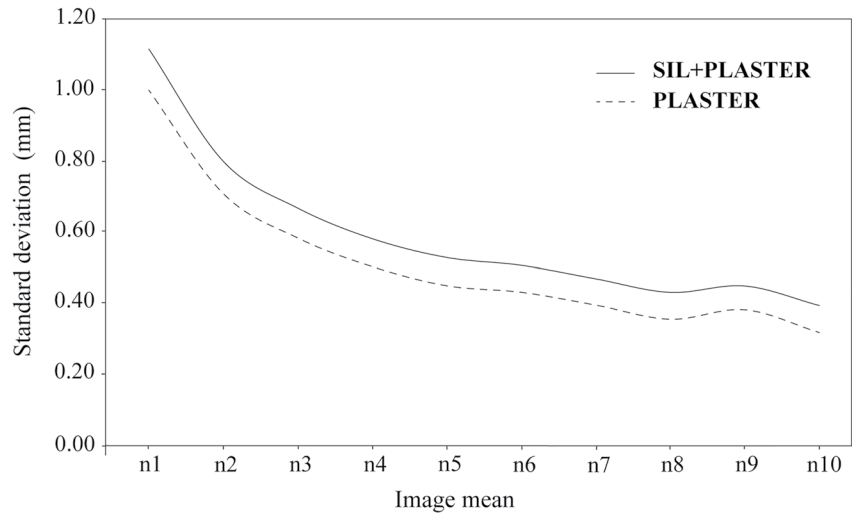
Figure 5. Variation of the standard deviation value obtained by averaging with different number of images for two different materials (PLASTER and Quartz sand (SIL) + PLASTER). Note that at both cases the main reduction of standard deviation value occurs for the averaging involving up to five images (n5).

Figure 6. Comparison of the standard deviation values obtained for all the experiments and the averaging of the results (using between 2 and 10 images) for all the materials tested. The *Y*-axis represents the value of the standard deviation in millimeters for each experiment and processing result. The x-axis shows, for each material, the four different acquisition distances at which the images have been recorded, with h1 being the height of the lesser distance (0.60 m) and h4 being the height of the greatest distance (1.05 m) from the Kinect to the material studied. Each material is represented with a gray intensity, making a graduated shading as the number of images involved in the averaging increases. The darkest tone represents the standard deviation of 1 single image (n1), while the lightest tone represents the standard deviation of the average of 10 consecutive images (n10) for each of the materials and each of the acquisition distances of the Kinect sensor.

Figure 7. Case study of monitoring of a tectonic model of shortening due to simple compression using Kinect v2 device. (a) Experimental design; (b) Kinect v2 RGB images of the model surface at the end of the experiment, where the asymmetric positive reliefs due to thrusting can be observed; (c) topography of the model at the end of the experiment obtained by Kinect v2 distance images; (d) topography of the model at the end of the experiment made form the average of the 6 last Kinect v2 distance images.
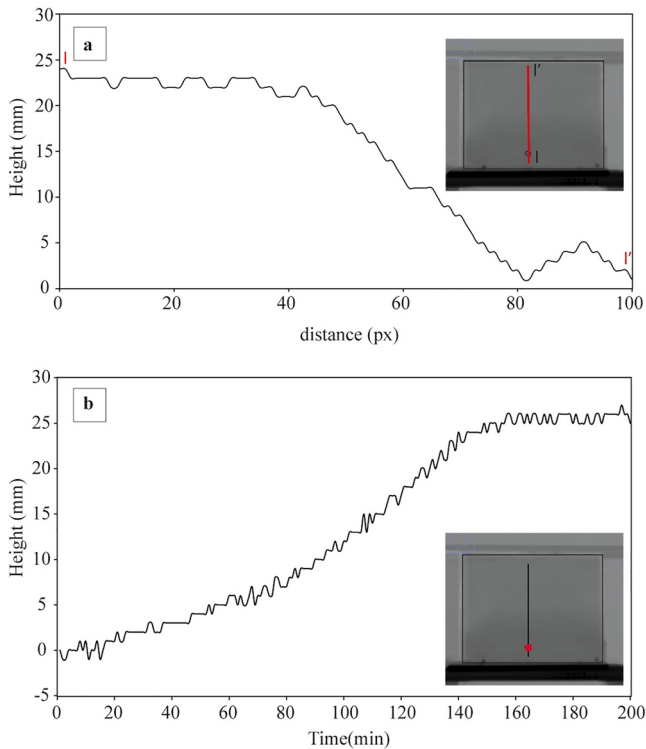
Figure 8. (a) Topographic profile across the center of the model at the end of the experiment extracted from the final Kinect v2 distance image. (b) Temporal profile of the evolution of the altitude of a point located at the lower part of the profile, obtained from the sequence of the Kinect v2 distance images of the experiment.

The ability of the Kinect v2 for easily producing useful DEMs in this kind of models is even clearer when topography change in the experiment is analyzed. Figure 10 A shows the topography difference between the final and the initial times of the experiment. An apparent subsidence of up to 8 mm can be observed at the summit zone, whereas an apparent uplift of up to 9 mm is visible at the upper left flank (Figure 10). Those deformed areas are clearly related to the deformation features visible at the final RGB image: the apparent subsidence coincides with the summit half-graben and is clearly bounded by the main curved scarp dipping toward the volcano interior, whereas the apparent uplift defines a bulge, the location of which coincides that of the strongly fractured zone (Figure 9b). The time-averaging filter clearly reduces the speckle pattern in the DEM (Figure 10b). The surface deformation detected by the Kinect v2 distance images in this model is quite similar to that observed in alike models with similar resolution monitored by using X-ray MDCT scanning techniques (Rincón et al., 2018).

## 6. Discussion: Advantages and Limitations of the Kinect v2 Device for Models Monitoring

Since the pioneering work of Tortini et al. (2014), RGB-D cameras have been used for monitoring volcanic and tectonic sandbox models in a short numbers of works. The Kinect v1 sensor has only been used only in the volcano tectonic models of Rincón et al. (2015) and Hyman and Bursik (2018), and the tectonic models of Tămas et al. (2019). We see several potential reasons that made modellers reluctant to use the Kinect v1 more extensively: the low resolution of the RGB camera, and the great sensitivity to light conditions, such that problems with light reflection lead to pixels values of zero (Rincón et al., 2015). The results from this work show than both problems have been resolved in new RGB-D cameras of the Kinect v2.

Our results also show that the color of the granular material has the strongest influence on the precision distance images measured with Kinect v2: black sand leads to much lower precision than the other materials (Figures 3 and 6). This has been previously noted by for example, Wasenmüller and Stricker (2016) who show that, for the same conditions, light color targets show a standard deviation of ~1 mm, whereas a black surface has a standard deviation of up to 4 mm. Since the granular materials most commonly used at volcanic and tectonic sandbox models are light colored, this feature is not an issue for using the Kinect v2 for monitoring sandbox experiments.

The results from our two different experiments (Section 5) show that the Kinect v2 is suitable for (a) properly monitoring hour- or minutes-long experiments in continuous mode (in a very simple way), and (b) detecting surface deformations of several millimeters only. The monitoring of these experiments by photogrammetric techniques using 4–5 synchronized cameras could provide horizontal and vertical resolutions ≤0.1 mm (see e.g., Galland et al., 2016), much higher than those obtained with the Kinect v2 device. Therefore, if the budget and the technical knowledge for using photogrammetric techniques are available, more precise monitoring results in sandbox experiments can be obtained by those techniques than using the Kinect v2. However, our results show that the Kinect v2 device, in combination with our KAM software, provides a low-cost, easy-of-use and robust solution for obtaining monitoring results with precisions ≤1 mm at a very high-rate in sandbox experiments. Given that sandbox experiments is also a powerful
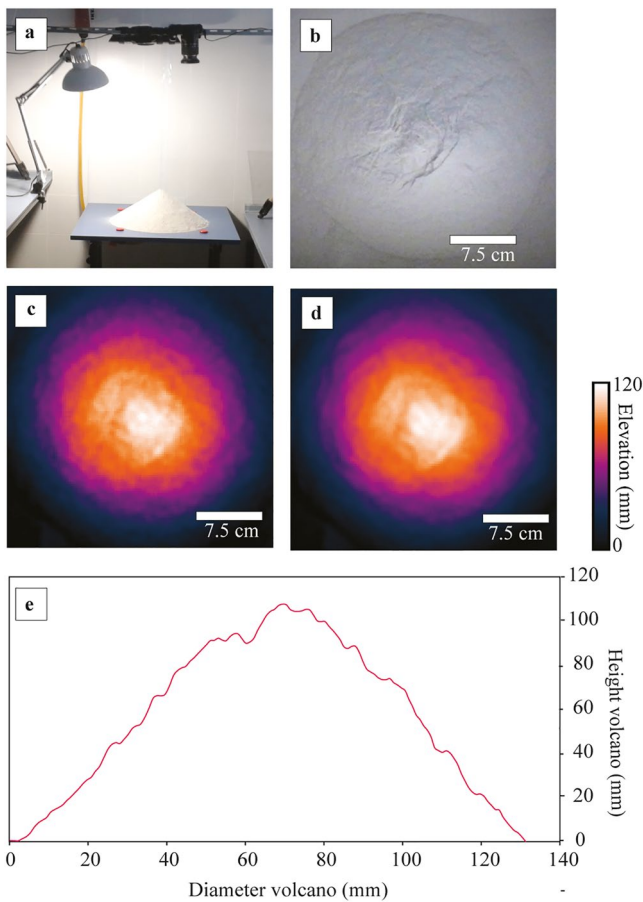
Figure 9. Case study of monitoring of a volcano topography during an intrusion experiment using Kinect v2 device. (a) Experimental design, with the sand + plaster cone, the tube used for syrup injection at the cone base and the monitoring device (Kinect v2 + digital camera) above the model; (b) Kinect v2 RGB images of the cone at the end of the experiment, where the faulting produced by the syrup intrusion can be observed; (c) topography of the cone at the end of the experiment obtained by Kinect v2 distance images; (d) Topography of the cone at the end of the experiment made form the average of the 7 last Kinect v2 distance images; (e) Topographic profile of the model shown in (d)
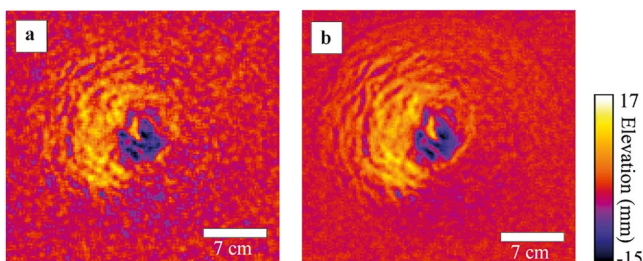
Figure 10. (a) Accumulated topographic changes at the cone produced during the experiment obtained by the subtraction of the last and first Kinect v2 distance images; (b) The same topographic changes obtained from the subtraction of the averaging of the 7 last distance images and the averaging of the 7 first distance images obtained with Kinect v2 device.

teaching tool, the Kinect v2 combined with our open-source KAM software offers a very affordable solution as an education tool at both high school and university levels.

Other volcano-tectonic experiments could be also potentially monitored using the Kinect v2 device, such as caldera collapse, volcano-fault interactions or volcano spreading processes (e.g., Cecchi et al., 2005; Delcamp et al., 2012; Grosse et al., 2020; Roche et al., 2001). Especially, those experiments focused on the applicability of analogue modeling for a better understanding of monitoring data of active volcanoes, which usually deal with fast but small surface deformations (i.e., uplifts of ≤ 3 mm in ≈ 10 s; e.g., Guldstrand et al., 2017, 2018). We suggest that the possible applicability of the Kinect v2 to monitoring those type of experiments is a promising research direction that can provide very interesting additional results.

Otherwise, the possible use of the Kinect v2 device for monitoring topographic evolution of tectonic-geomorphology experiments using water-saturated granular materials (e.g., Graveleau et al., 2011, 2012) requires a more detailed exploration. In those experiments the uppermost 1–2 mm of the model surface needs to dry before the use of laser interferometer or laser scanner techniques, in order to avoid bright laser points that could affect DEM precision, which implies that the experiment must be stopped (Reitano et al., 2020; Viaplana-Muzas et al., 2015). A detailed study comparing dry and water-saturated granular materials response to the Kinect v2 measurements is therefore needed to check the suitability of the Kinect v2 for a dynamic monitoring (i.e., avoiding to stop the experiment) of this kind of models, which could be a very useful application of the Kinect v2.

7. Future Improvements of the Kinect v2 Monitoring of Analogue Models

7.1. Time-Filtering Methodologies

The results from this work show that the averaging of several consecutive images is a powerful tool for reducing the noise of the distance images obtained with the Kinect v2 device and increase their precision. However, for applying this technique to the entire set of an experiment, special attention must be taken to the relationship between the number of images involved in the averaging (i.e., the time of the experiment that we are averaging) and the surface deformation rate. Otherwise, an unreal smoothing of the deformation rate can be produced, especially when topographic scarps initiate at the experiment surface. Anyway, the oscillating nature of the distance values obtained for each pixel in several consecutive images (Figure 2), opens the possibility to future exploration of the application of more sophisticated tools of signal temporal filtering to the distance the Kinect v2 data, such as a Kalman filter or temporal denoising Smoothed Pointing filtering (e.g., Essmaeel et al., 2012).

7.2. RGB-D Time-of-Flight Devices

Our results show that RGB-D sensors are powerful tools for monitoring analogue models and, with the evolution of the technology, the precisions acquired will be probably much better than those currently achieved. Although in October 2017 Microsoft® stopped manufacturing the two versions of the Kinect sensor, betting on augmented reality for videogames, the Kinect v2 devices are still available in the market. In addition, the Kinect
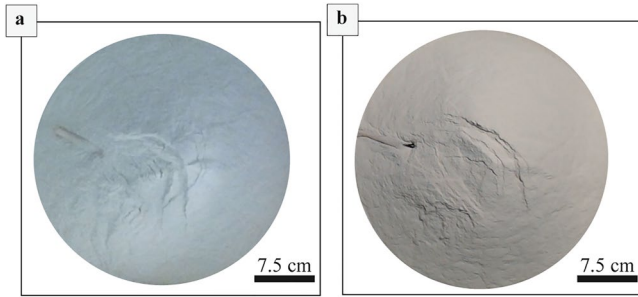
Figure 11. RedGreenBlue (RGB) images obtained by monitoring two experiments of a volcano-intrusion model (similar to that of Figure 9) with Kinect Acquisition for Analogue Models software using: (a) the RGB camera of Kinect v2 device, and (b) a webcam (Logitech HD PRO WEBCAM C920) connected to the same computer than Kinect v2. Despite the higher spatial resolution obtained with the webcam (≈0.3 mm/px vs. ≈0.5 mm/px), it can be observed that Kinect v2 RGB camera still allows for a proper visual interpretation of the deformation features at the model surface.

Azure was launched in February 2019, with similar technology as that of the Kinect v2, but with some improved specifications and the possibility to use different acquisition modes depending on the needs of the user. The Kinect Azure exhibits spatial resolutions in the distance camera up to 1 Megapixel ($1,024 \times 1,024$ px vs. 512×424 of the Kinect v2) and in the RGB camera up to 12 Megapixels ($4,096 \times 3,072$ px vs. $1,920 \times 1,080$ of the Kinect v2). However, due to the wider Field-of-View of the Kinect Azure cameras, although the spatial resolution of the RGB camera has improved (at 0.6 m above the models: ~0.3 vs. ~0.5 mm for the Kinect v2), the pixel resolution of the distance camera of the Kinect Azure is lower (~2 vs. ~1.6 mm for the Kinect v2 also at 0.6 m above the models). Anyway, the expected precision of the vertical displacement should be the same between the Kinect Azure and those presented in this work, since the technology of the distance sensor is the same.

Other RGB-D devices can be used for similar purposes. Based on time-of-flight technology similar to the Kinect v2 (and with similar prices), several devices are also available and could be a promising research avenue for analogue models monitoring since some of them have in theory better resolution than the Kinect v2 cameras. ASUS Xtion 2 holds a RGB camera with a better resolution ($2,592 \times 1,944$ pixels) but its ToF distance camera produces 640×480 pixel images from the interpolation of actual 320×240 pixel images (therefore worse than the 512×424 of the Kinect v2). Basler ToF-6 m camera has 640×480 pixel resolution for both the RGB and distance cameras, so the theorical resolution of its distance camera is ≈0.7 mm. BlasterX Senz 3D has a RGB camera similar to the Kinect v2 ($1,920 \times 1,080$) but its 640×480 distance image, a 60 frames-per-second rate and a minimum range of just 0.2 m. The theorical resolution of its distance camera is ≈0.4 mm, with ≈0.2 mm for the RGB camera. A similar study of its response to different experiment materials should be performed in order to fully evaluate their capabilities.

7.3. Measurements of Horizontal and Vertical Model Displacements With the Kinect v2

The calculation of the model deformation using the Kinect v2 (and the rest of the RGB-D sensors) is realized by subtracting DEMs obtained at different times (see e.g., Figure 10). That deformation is a result of both vertical and horizontal displacements of the model surface, since the simple DEM subtraction does not allow the separation of the vertical versus horizontal components of the surface displacements. The potential for using RGB cameras for computing horizontal displacements maps of the model surfaces using PIV techniques, synchronized with the Kinect v2 DEMs, is another venue for future exploration for a more complete monitoring of the surface deformation of sandbox models. This would potentially require only one camera (in addition to the Kinect v2 device) mounted vertically above the setup (see e.g., Delcamp et al., 2008). The spatial resolution of horizontal displacements measurements using PIV techniques depends both on the cross-correlation algorithm used and the resolution of the camera system. The spatial resolution of the Kinect v2 RGB camera (≥0.5 mm, Table 2), although good enough for visual identification and mapping of faults and other deformation features on the model surfaces (Figures 7 and 9), is low for obtaining useful horizontal displacements by PIV analysis.

Our KAM software provides a potential way to explore this field, due to its capacity for obtaining simultaneous distance images with the Kinect v2 and RGB images with any other camera connected to the computer. As an example, we have repeated an intrusion experiment, similar to that shown Section 5.2, and monitored it using KAM software, in one case using the Kinect v2 RGB camera and at the second test using a $1,920 \times 1,080$ pixels Logitech HD PRO WEBCAM C920 (Figure 11). The spatial resolution of the model surface images obtained with that webcam at 0.8 m height is ≈0.3 mm/px, but despite that higher spatial resolution, which clearly eases the model visual interpretation, it can be observed that the Kinect v2 RGB camera still allows for a proper visual interpretation of the deformation features at the model surface (Figures 11a vs. 11b). Lighting conditions in the laboratory depending of the experiment set-up are also important for that visual interpetation of the images. This submilimiter resolution is still lower than those of the images commonly used for PIV analysis obtained with SLR digital cameras in similar models (e.g., Galland et al., 2016). However, current 4 K ($4,096 \times 2,160$ pixels)

webcams with optical zoom (e.g., Logitech BRIO ULTRA HD PRO WEBCAM) could potentially allow to obtain RGB images of the experiments with a horizontal resolution <0.2 mm, which could be theorically high enough to allow the monitoring of horizontal displacements with PIV techniques. However, a detailed study about the effect of the possible distortions of those images and their needed co-registration with the Kinect v2 distance images is needed. The possibility to obtain, with the simple KAM software and cheap the Kinect v2 device coupled to a webcam, both DEMs and horizontal displacements maps of sandbox analogue models could produce very promising results.

8. Conclusions

1. The Kinect v2 device is an easy and powerful tool for monitoring topography change in sandbox analogue models made of granular materials.
2. Using the Kinect v2, consecutive DEMs of the models can be obtained in a very simple way, with an horizontal resolution of ~1.6 mm and vertical-precisions of 1.0–1.5 mm. Those DEMs can be acquired with a high temporal resolution (more than 10 images per second). Optical images of the model surface (with horizontal resolution of ~0.5 mm) can be obtained simultaneously.
3. Our publicy avalilable software KAM facilitates the use of the Kinect v2 for monitoring analogue models, allowing: (a) to choose the optical camera used for capturing the RGB images (which can allow increase their horizontal resolution) and crop the region-of-interest; (b) to choose the frame rate for both the distance and RGB images; and (c) to optionally perform a later customized averaging of the distance images obtained.
4. This option of applying a time-filtering to the Kinect v2 distance images allows increasing the precision of the DEMs of the models, obtaining by averaging just 5 consecutive images precisions up to ≤0.5 mm.
5. Amongst the parameters studied (relief of the experiments, type of material and distance from the sensor), the type of material is the most influential on the precision of the data. Therefore, before the monitoring of analogue models with the Kinect v2 sensor, it is essential to consider the physical characteristics of the experimental materials.
6. The existence of an initial topography in the experiment does not influence the precision of the distance data, which is a key aspect in all those experiments dealing with the evaluation of changes in the topography of volcanic edifices.
7. The Kinect v2 sensor can therefore produce DEMs of sandbox analogue models with better time-resolution and slightly lower spatial and vertical resolution than more complex and expensive systems such as lasers, systems based on structured light or photogrammetry. But probably its major advantages are its low price, its ease of use and the almost total absence of need for processing of data in order to obtain the DEMs of the model.
8. If the budget and/or the technical knowledge for using precise monitoring techniques (e.g., photogrammetry) are not available, the Kinect v2 in combination with KAM software is a powerful and easy tool for acquiring quantitative data of surface deformation in sandbox analogue models. We hope that these results encourage analogue modellers to use the Kinect v2 for the monitoring of their experiments (alone or in combination with other systems) and for further exploring new research questions and set-up ideas. Besides, we expect that our results encourage other researchers to become new analogue modellers.

Data Availability Statement

Software Kinect Acquisition for Analogue Models (KAM) is available at https://doi.org/10.5281/zenodo.3956392.

References

Abdelmalak, M. M., Bulois, C., Mourgues, R., Galland, O., Legland, J. B., & Gruber, C. (2016). Description of new dry granular materials of variable cohesion and friction coefficient: Implications for laboratory modeling of the brittle crust. *Tectonophysics*, *684*, 39–51. https://doi.org/10.1016/j.tecto.2016.03.003

Agostini, A., Corti, G., Zeoli, A., & Mulugeta, G. (2009). Evolution, pattern, and partitioning of deformation during oblique continental rifting: Inferences from lithospheric-scale centrifuge models. *Geochemistry, Geophysics, Geosystems*, *10*(11). https://doi.org/10.1029/2009gc002676

Beckett, F. M., Mader, H. M., Phillips, J. C., Rust, A. C., & Witham, F. (2011). An experimental study of low-Reynolds-number exchange flow of two Newtonian fluids in a vertical pipe. *Journal of Fluid Mechanics*, *682*, 652–670. https://doi.org/10.1017/jfm.2011.264

Bertelsen, H. S., Guldstrand, F., Sigmundsson, F., Pedersen, R., Mair, K., & Galland, O. (2021). Beyond elasticity: Are Coulomb properties of the Earth's crust important for volcano geodesy? *Journal of Volcanology and Geothermal Research*, *410*, 107153. https://doi.org/10.1016/j.jvolgeores.2020.107153

Cecchi, E., van Wyk de Vries, B., & Lavest, J. M. (2005). Flank spreading and collapse of weak-cored volcanoes. *Bulletin of Volcanology*, *67*(1), 72–91. https://doi.org/10.1007/s00445-004-0369-3

Delcamp, A., van Wyk de Vries, B., & James, M. R. (2008). The influence of edifice slope and substrata on volcano spreading. *Journal of Volcanology and Geothermal Research*, *177*(4), 925–943. https://doi.org/10.1016/j.jvolgeores.2008.07.014

Delcamp, A., van Wyk de Vries, B., James, M. R., Gailler, L. S., & Lebas, E. (2012). Relationships between volcano gravitational spreading and magma intrusion. *Bulletin of Volcanology*, *74*(3), 743–765. https://doi.org/10.1007/s00445-011-0558-9

Dutta, T. (2012). Evaluation of the Kinect™ sensor for 3-D kinematic measurement in the workplace. *Applied Ergonomics*, *43*(4), 645–649. https://doi.org/10.1016/j.apergo.2011.09.011

Ernst, F., & Saß, P. (2015). Respiratory motion tracking using Microsoft's Kinect v2 camera. *Current Directions in Biomedical Engineering*, *1*(1), 192–195. https://doi.org/10.1515/cdbme-2015-0048

Essmaeel, K., Gallo, L., Damiani, E., De Pietro, G., & Dipandà, A. (2012). Temporal denoising of kinect depth data. In *Eighth International Conference on Signal Image Technology and Internet Based Systems* (pp. 47–52). https://doi.org/10.1109/SITIS.2012.18

Fedorik, J., Zwaan, F., Schreurs, G., Toscani, G., Bonini, L., & Seno, S. (2019). The interaction between strike-slip dominated fault zones and thrust belt structures: Insights from 4D analogue models. *Journal of Structural Geology*, *122*, 89–105. https://doi.org/10.1016/j.jsg.2019.02.010

Fittipaldi, M., Urbani, S., Neri, M., Trippanera, D., & Acocella, V. (2019). Understanding the origin of magmatic necks: Insights from Mt. Etna volcano (Italy) and analogue models. *Bulletin of Volcanology*, *81*(2), 11. https://doi.org/10.1007/s00445-019-1273-1

Galland, O. (2012). Experimental modelling of ground deformation associated with shallow magma intrusions. *Earth and Planetary Science Letters*, *317*, 145–156. https://doi.org/10.1016/j.epsl.2011.10.017

Galland, O., Bertelsen, H. S., Guldstrand, F., Girod, L., Johannessen, R. F., Bjugger, F., et al. (2016). Application of open-source photogrammetric software MicMac for monitoring surface deformation in laboratory models. *Journal of Geophysical Research: Solid Earth*, *121*(4), 2852–2872. https://doi.org/10.1002/2015JB012564

Galland, O., Holohan, E., van Wyk deVries, B., & Burchardt, S. (2018). Laboratory modelling of volcano plumbing systems: A review. In *Physical geology of shallow magmatic systems* (pp. 147–214). Springer. https://doi.org/10.1007/11157_2015_9

Gonzalez-Jorge, H., Rodríguez-González, P., Martínez-Sánchez, J., González-Aguilera, D., Arias, P., Gesto, M., & Díaz-Vilariño, L. (2015). Metrological comparison between Kinect I and Kinect II sensors. *Measurement*, *70*, 21–26. https://doi.org/10.1016/j.measurement.2015.03.042

Graveleau, F., Hurtrez, J. E., Dominguez, S., & Malavieille, J. (2011). A new experimental material for modeling relief dynamics and interactions between tectonics and surface processes. *Tectonophysics*, *513*(1–4), 68–87. https://doi.org/10.1016/j.tecto.2011.09.029

Graveleau, F., Malavieille, J., & Dominguez, S. (2012). Experimental modelling of orogenic wedges: A review. *Tectonophysics*, *538*, 1–66. https://doi.org/10.1016/j.tecto.2012.01.027

Gressier, J. B., Mourgues, R., Bodet, L., Matthieu, J. Y., Galland, O., & Cobbold, P. (2010). Control of pore fluid pressure on depth of emplacement of magmatic sills: An experimental approach. *Tectonophysics*, *489*(1–4), 1–13. https://doi.org/10.1016/j.tecto.2010.03.004

Grosse, P., Poppe, S., Delcamp, A., van Wyk deVries, B., & Kervyn, M. (2020). Volcano growth versus deformation by strike-slip faults: Morphometric characterization through analogue modelling. *Tectonophysics*, *781*, 228411. https://doi.org/10.1016/j.tecto.2020.228411

Guldstrand, F., Burchardt, S., Hallot, E., & Galland, O. (2017). Dynamics of surface deformation induced by dikes and cone sheets in a cohesive Coulomb brittle crust. *Journal of Geophysical Research: Solid Earth*, *122*(10), 8511–8524. https://doi.org/10.1002/2017JB014346

Guldstrand, F., Galland, O., Hallot, E., & Burchardt, S. (2018). Experimental constraints on forecasting the location of volcanic eruptions from pre-eruptive surface deformation. *Frontiers of Earth Science*, *6*, 7. https://doi.org/10.3389/feart.2018.00007

Hall, J. (1815). II. On the vertical position and convolutions of certain strata, and their relation with granite. *Earth and Environmental Science Transactions of the Royal Society of Edinburgh*, *7*(1), 79–108. https://doi.org/10.1017/s0080456800019268

Hatem, A. E., Cooke, M. L., & Madden, E. H. (2015). Evolving efficiency of restraining bends within wet kaolin analog experiments. *Journal of Geophysical Research: Solid Earth*, *120*(3), 1975–1992. https://doi.org/10.1002/2014jb011735

Hubbert, M. K. (1937). Theory of scale models as applied to the study of geologic structures. *Bulletin of the Geological Society of America*, *48*(10), 1459–1520. https://doi.org/10.1130/gsab-48-1459

Hyman, D., & Bursik, M. (2018). Deformation of volcanic materials by pore pressurization: Analog experiments with simplified geometry. *Bulletin of Volcanology*, *80*(3), 19. https://doi.org/10.1007/s00445-018-1201-9

Jiao, J., Yuan, L., Tang, W., Deng, Z., & Wu, Q. (2017). A post-rectification approach of depth images of Kinect v2 for 3D reconstruction of indoor scenes. *ISPRS International Journal of Geo-Information*, *6*(11), 349. https://doi.org/10.3390/ijgi6110349

Kadambi, A., Bhandari, A., & Raskar, R. (2014). *3D Depth cameras in vision: Benefits and limitations of the hardware*. In *Computer Vision and Machine Learning with RGB-D Sensors* (Vol. 3–26). Springer.

Kavanagh, J. L., Engwell, S. L., & Martin, S. A. (2018). A review of laboratory and numerical modelling in volcanology. *Solid Earth*, *9*(2), 531–571. https://doi.org/10.5194/se-9-531-2018

Kavanagh, J. L., Menand, T., & Daniels, K. A. (2013). Gelatine as a crustal analogue: Determining elastic properties for modelling magmatic intrusions. *Tectonophysics*, *582*, 101–111. https://doi.org/10.1016/j.tecto.2012.09.032

Lachat, E., Macher, H., Landes, T., & Grussenmeyer, P. (2015). Assessment and calibration of a RGB-D camera (Kinect v2 Sensor) towards a potential use for close-range 3D modelling. *Remote Sensing*, *7*(10), 13070–13097. https://doi.org/10.3390/rs71013070

Liu, Y. K., Ruch, J., Vasyura-Bathke, H., & Jonsson, S. (2019). Influence of ring faulting in localizing surface deformation at subsiding calderas. *Earth and Planetary Science Letters*, *526*, 115784. https://doi.org/10.1016/j.epsl.2019.115784

Poppe, S., Holohan, E. P., Galland, O., Buls, N., Van Gompel, G., Keelson, B., et al. (2019). An inside perspective on magma intrusion: Quantifying 3D displacement and strain in laboratory experiments by dynamic X-ray computed tomography. *Frontiers of Earth Science*, *7*, 62. https://doi.org/10.3389/feart.2019.00062

Poppe, S., Holohan, E. P., Rudolf, M., Rosenau, M., Galland, O., Delcamp, A., & Kervyn, M. (2021). Mechanical properties of quartz sand and gypsum powder (plaster) mixtures: Implications for laboratory model analogues for the Earth's upper crust. *Tectonophysics*, *814*, 228976. https://doi.org/10.1016/j.tecto.2021.228976

Pysklywec, R. N., & Cruden, A. R. (2004). Coupled crust-mantle dynamics and intraplate tectonics: Two-dimensional numerical and three-dimensional analogue modeling. *Geochemistry, Geophysics, Geosystems*, *5*(10). https://doi.org/10.1029/2004gc000748

Reber, J. E., Cooke, M. L., & Dooley, T. P. (2020). What model material to use? A Review on rock analogs for structural geology and tectonics. *Earth-Science Reviews*, *202*, 103107. https://doi.org/10.1016/j.earscirev.2020.103107

Reitano, R., Faccenna, C., Funiciello, F., Corbi, F., & Willett, S. D. (2020). Erosional response of granular material in landscape models. *Earth Surface Dynamics*, *8*(4), 973–993. https://doi.org/10.5194/esurf-8-973-2020

Rincón, M., Márquez, A., Herrera, R., Alonso-Torres, A., Granja-Bruña, J. L., & van Wyk deVries, B. (2018). Contrasting catastrophic eruptions predicted by different intrusion and collapse scenarios. *Scientific Reports*, *8*(1), 1–11. https://doi.org/10.1038/s41598-018-24623-5

Rincón, M., Márquez, A., van Wyk deVries, B., Herrera, R., Granja Bruña, J. L., & Llanes Estrada, P. (2015). Aplicación del sensor Kinect en modelos análogos para la identificación morfo-estructural de procesos de deformación en volcanes. *Geogaceta*(57), 107–110.

Ritter, M. C., Leever, K., Rosenau, M., & Oncken, O. (2016). Scaling the sandbox—Mechanical (dis) similarities of granular materials and brittle rock. *Journal of Geophysical Research: Solid Earth*, *121*(9), 6863–6879. https://doi.org/10.1002/2016jb012915

Roche, O., & Carazzo, G. (2019). The contribution of experimental volcanology to the study of the physics of eruptive processes, and related scaling issues: A review. *Journal of Volcanology and Geothermal Research*, *384*, 103–150. https://doi.org/10.1016/j.jvolgeores.2019.07.011

Roche, O., van Wyk deVries, B., & Druitt, T. H. (2001). Sub-surface structures and collapse mechanisms of summit pit craters. *Journal of Volcanology and Geothermal Research*, *105*(1–2), 1–18. https://doi.org/10.1016/S0377-0273(00)00248-1

Sarbolandi, H., Lefloch, D., & Kolb, A. (2015). Kinect range sensing: Structured-light versus Time-of-Flight Kinect. *Computer Vision and Image Understanding*, *139*, 1–20. https://doi.org/10.1016/j.cviu.2015.05.006

Schellart, W. P. (2000). Shear test results for cohesion and friction coefficients for different granular materials: Scaling implications for their usage in analogue modelling. *Tectonophysics*, *324*(1–2), 1–16. https://doi.org/10.1016/S0040-1951(00)00111-6

Schellart, W. P., & Strak, V. (2016). A review of analogue modelling of geodynamic processes: Approaches, scaling, materials and quantification, with an application to subduction experiments. *Journal of Geodynamics*, *100*, 7–32. https://doi.org/10.1016/j.jog.2016.03.009

Schrank, C. E., & Cruden, A. R. (2010). Compaction control of topography and fault network structure along strike-slip faults in sedimentary basins. *Journal of Structural Geology*, *32*(2), 184–191. https://doi.org/10.1016/j.jsg.2009.11.003

Schreurs, G., Buiter, S. J., Boutelier, J., Burberry, C., Callot, J. P., Cavozzi, C., et al. (2016). Benchmarking analogue models of brittle thrust wedges. *Journal of Structural Geology*, *92*, 116–139. https://doi.org/10.1016/j.jsg.2016.03.005

Tămaş, D. M., Schléder, Z., Tămaş, A., Krézsek, C., Copoţ, B., & Filipescu, S. (2019). Middle Miocene evolution and structural style of the Diapir Fold Zone, Eastern Carpathian Bend Zone, Romania: Insights from scaled analogue modelling. *Geological Society, London, Special Publications*, *490*, 267–284. https://doi.org/10.1144/SP490-2019-091

Terven, J. R., & Córdova-Esparza, D. M. (2016). Kin2. A Kinect 2 toolbox for MATLAB. *Science of Computer Programming*, *130*, 97–106. https://doi.org/10.1016/j.scico.2016.05.009

Toeneboehn, K., Cooke, M. L., Bemis, S. P., Fendick, A. M., & Benowitz, J. (2018). Stereovision Combined with particle tracking velocimetry reveals advection and uplift within a restraining bend simulating the Denali fault. *Frontiers of Earth Science*, *6*, 152. https://doi.org/10.3389/feart.2018.00152

Tortini, R., Bonali, F. L., Corazzato, C., Carn, S. A., & Tibaldi, A. (2014). An innovative application of the Kinect in Earth sciences: Quantifying deformation in analogue modelling of volcanoes. *Terra Nova*, *26*(4), 273–281. https://doi.org/10.1111/ter.12096

Trippanera, D., Ruch, J., Acocella, V., & Rivalta, E. (2015). Experiments of dike-induced deformation: Insights on the long-term evolution of divergent plate boundaries. *Journal of Geophysical Research: Solid Earth*, *120*(10), 6913–6942. https://doi.org/10.1002/2014JB011850

Viaplana-Muzas, M., Babault, J., Dominguez, S., Van Den Driessche, J., & Legrand, X. (2015). Drainage network evolution and patterns of sedimentation in an experimental wedge. *Tectonophysics*, *664*, 109–124. https://doi.org/10.1016/j.tecto.2015.09.007

Von Hagke, C., Kettermann, M., Bitsch, N., Bücken, D., Weismüller, C., & Urai, J. L. (2019). The effect of obliquity of slip in normal faults on distribution of open fractures. *Frontiers of Earth Science*, *7*, 18. https://doi.org/10.3389/feart.2019.00018

Wasenmüller, O., & Stricker, D. (2016). Comparison of kinect v1 and v2 depth images in terms of accuracy and precision. In *Asian conference on computer vision* (pp. 34–45). Springer. https://doi.org/10.1007/978-3-319-54427-4_3

Xia, J., & Siochi, R. A. (2012). A real-time respiratory motion monitoring system using KINECT: Proof of concept. *Medical Physics*, *39*(5), 2682–2685. https://doi.org/10.1118/1.4704644

Zwaan, F., Schreurs, G., & Rosenau, M. (2020). Rift propagation in rotational versus orthogonal extension: Insights from 4D analogue models. *Journal of Structural Geology*, *135*, 103946. https://doi.org/10.1016/j.jsg.2019.103946